Supporting Information for

Observation of Optical Anisotropy and a Linear Dichroism Transition in Layered Silicon Phosphide

Xing Xie[1,2], Junnan Ding[1,2], Biao Wu[1,2], Haihong Zheng[1,2], Shaofei Li[1], Chang-Tian Wang[3,4], Jun He[1], Zongwen Liu[5,6], Jian-Tao Wang[3,4,7], Ji-an Duan[2], and Yanping Liu[1,2,8*]

1. *School of Physics and Electronics, Hunan Key Laboratory for Super-microstructure and Ultrafast Process, Central South University, 932 South Lushan Road, Changsha, Hunan 410083, People's Republic of China*
2. *State Key Laboratory of High-Performance Complex Manufacturing, Central South University, 932 South Lushan Road, Changsha, Hunan 410083, People's Republic of China*
3. *Beijing National Laboratory for Condensed Matter Physics, Institute of Physics, Chinese Academy of Sciences, Beijing 100190, People's Republic of China*
4. *School of Physical Sciences, University of Chinese Academy of Sciences, Beijing 100049, People's Republic of China*
5. *School of Chemical and Biomolecular Engineering, The University of Sydney, NSW 2006, Australia*
6. *The University of Sydney Nano Institute, The University of Sydney, NSW 2006 Australia*
7. *Songshan Lake Materials Laboratory, Dongguan, Guangdong 523808, People's Republic of China*
8. *Shenzhen Research Institute of Central South University, Shenzhen 518057, People's Republic of China*

* Correspondence and requests for materials should be addressed to email: liuyanping@csu.edu.cn

Outline:

1. Crystal structural information of SiP

To calculate the vibrational patterns, Raman spectra, band structures, and elastic constants of bulk SiP, we relaxed the lattice constants and atomic positions of bulk SiP, until the force on atoms was less than 0.02 eV/Å. To correct the effect of the van der Waals interaction, the Grimme DFT-D3[1] method was adopted while relaxing the crystal structure. The relaxed lattice parameters and Wyckoff positions of bulk SiP were listed in Table S1. Our calculated lattice constant is in agreement with the previously calculated results[2]. The bulk SiP with space group of $Cmc2_1$ has six inequivalent Si and P sites (named as Si1-Si6 and P1-P6, respectively), and the crystal structure of bulk SiP can be reproduced using the given information listed in Table S1.

Table S1. The calculated lattice parameters and Wyckoff positions of bulk SiP with space group $Cmc2_1$. Bulk SiP crystallized orthorhombic symmetry has six respective inequivalent Si and P sites, which all occupy the 4a site.

Space Group	Lattice Constants (Å)	Wyckoff Position				
		atom	position	x	y	z
$Cmc2_1$	a= 3.521, b=20.517, c=13.780 $\alpha=\beta=\gamma=90°$	Si1	4a	0.0000	0.1710	0.7379
		Si2	4a	0.0000	0.0597	0.7795
		Si3	4a	0.0000	0.4354	0.6811
		Si4	4a	0.0000	0.4325	0.8515
		Si5	4a	0.5000	0.2953	0.8358
		Si6	4a	0.5000	0.2981	0.6656
		P1	4a	0.0000	0.2312	0.8789
		P2	4a	0.0000	0.3445	0.5874
		P3	4a	0.5000	0.4997	0.6381
		P4	4a	0.5000	0.0412	0.8815
		P5	4a	0.5000	0.1893	0.6360
		P6	4a	0.5000	0.3862	0.9296

2. Raman spectra of SiP flakes

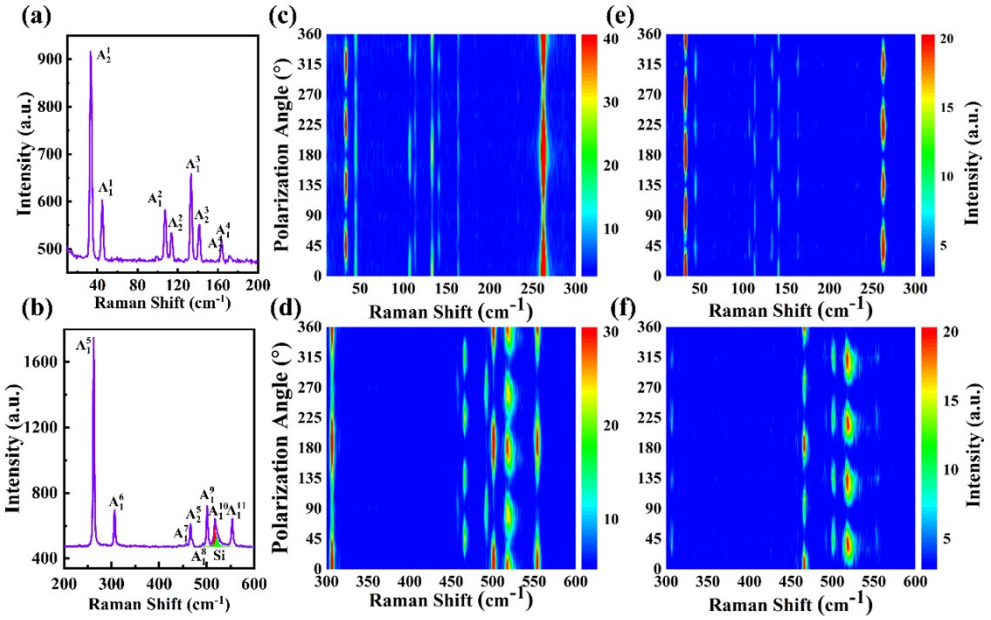

Figure S1. Raman spectra of layered SiP materials. (a) 10-200 cm^{-1} and (b) 200-600 cm^{-1} Raman spectra of SiP flakes. The Raman active modes are labelled in pictures (a) and (b). Two shear modes are identified as A_2^1 and A_1^1 modes. The peaks filled red (517 cm^{-1}) and green (521 cm^{-1}) were identified as A_1^{10} and Si Raman modes. (c), (d) parallel- and (e), (f) cross-polarization-resolved Raman spectra as a function of polarizing angle with the wavenumber range of (c), (e) 10-300 cm^{-1} and (d), (f) 300-600 cm^{-1}. The periodic spots of A_1 modes are different from those of A_2 modes, and the stripes under parallel polarization configuration show distinct to those under cross-polarization configuration.

As displayed in Figure S1a and S1b, sixteen Raman peaks of SiP flakes and one peak of Si wafer are observed. For the wavenumber range of 100-600 cm^{-1}, the measured Raman peaks are consistent with the previous Raman study[3-5] (see Figure S2). To identify the Raman modes, the Raman spectrum of bulk SiP was calculated based on density functional theory (DFT). According to the discussion of Raman intensity in the backscattering configuration and the theoretical Raman spectra (Figure S2), A_2 modes had five peaks, while A_1 modes had eleven peaks. Their atomic vibrational patterns are exhibited in Figure S3. The A_1 modes showed the atomic vibrational directions in the (100) plane, while the atoms vibrated along the [100]

direction for A_2 modes. As shown in Figure S1a, two low-wavenumber Raman active modes (<100 cm^{-1}) of A_2^1 and A_1^1 with the wavenumber of 32 cm^{-1} and 44 cm^{-1}, respectively, are observed. These two low-frequency Raman modes exhibited relative atomic vibration between layers with the vibrational direction in in-plane, indicating that A_2^1 and A_1^1 modes belong to shear vibrational modes. Compared with bulk $PdSe_2$ that did not observe the shear modes[6], the shear vibrational modes of SiP flakes were evidently measured. The Raman spectra of SiP flakes, however, did not exhibit the breathing mode, which is an interlayer vibrational mode wherein the atoms move each other between layers with the direction in out-of-plane, as they belong to B_2 modes.

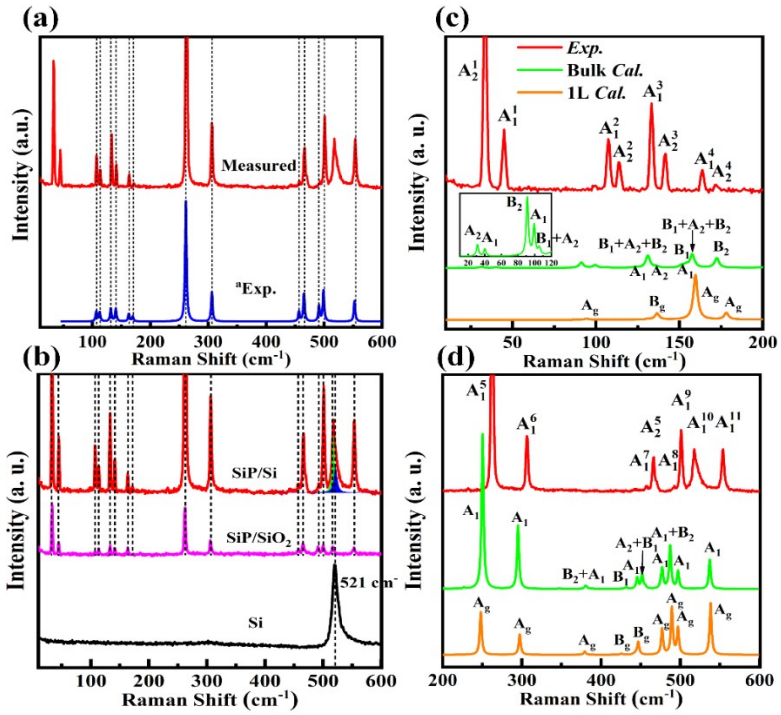

Figure S2. Experimental and theoretical Raman spectra of SiP flakes. (a) Raman spectra of SiP flakes measured in this work (red line) and the other result (blue line). Our results are in good agreement with the previous results[3] in the wavenumber range of 100-600 cm^{-1}. (b) Measured Raman spectrum of SiP flakes on Si (red line) and SiO_2 (pink line) substrates as well as the Raman spectrum of Si wafer (black line). The Raman peaks measured on Si substrate is consistent with that on SiO_2 substrate. (c) and (d) Experimental (red line) and theoretical (green line for bulk and orange for monolayer (1L)) Raman spectra for 10-200 cm^{-1} and 200-600 cm^{-1} wavenumber, respectively. The modes are marked on the corresponding peaks. The inset in

(c) is the enlarged experimental Raman spectra from 10 cm^{-1} to 120 cm^{-1} wavenumbers. [a]Ref[3]

In the high-frequency Raman spectra (>100 cm^{-1}), the observed ten A_1 and four A_2 modes could be divided into three vibrational cases. A_1^2, A_2^2, A_1^3, A_2^3, A_1^4, A_2^4, A_2^5, A_1^8, and A_1^9 modes were contributed by the motion of both Si and P atoms. It suggested that the associated movement of Si and P atoms could cause a wide range of wavenumber from 107 cm^{-1} to 501 cm^{-1}. While the A_1^5 and A_1^6 modes, which were located at 262 cm^{-1} and 306 cm^{-1}, respectively, were mainly derived from the movement of P atoms (Figure S3). Owing to the large polarization tensors caused by the movement of P atoms, the A_1^5 mode showed the highest intensity (~1270 a.u.) that was approximately 3 times higher than that of A_2^1 peak (~440 a.u.), which was the second-highest peak in this experiment's result. On the contrary, the A_1^7, A_1^{10}, and A_1^{11} modes at a wavenumber of 456, 517, and 554 cm^{-1}, respectively, mainly originated from the vibration of Si atoms with a slight movement of P atoms. The A_1^7 and A_1^{10} modes were mainly contributed by the relative motion of Si atoms in the Si1-Si1 bonds, whereas the A_1^{11} mode was derived from the relative movement of Si atoms in the Si2-Si2 bonds, suggesting that the stronger Si-Si interaction could scatter the light of larger wavenumbers. Notably, the A_1^{10} mode (517 cm^{-1}) was very close to the Raman peak of Si[7] (521 cm^{-1}, see Figure S2) due to the analogous bond lengths between Si (2.368 Å) and SiP (Si1-Si1 bond lengths of 2.362 Å).

The bulk SiP with a point group of C_{2v} possesses A_1, A_2, B_1, and B_2 Raman active modes. For the A_1 and B_2 modes, their atoms vibrate in the b-c plane. The A_1 modes have the vibration vectors of (0, -1, 1) on the atomic position of (0, y, z) and of (0, 1, 1) on the atomic position of (0, -y, z+1/2). While on corresponding atomic positions they have vibration vectors of (0, 1, 1) and (0, 1, -1), respectively, for B_2 modes. For A_2 and B_1 modes, the Si and P atoms move along [100] direction. On the atomic position of (0, y, z) and (0, -y, z+1/2), A_2 modes exhibit contrary orientation of movement (i.e., vibration vectors of (0, 0, 1) and (0, 0, -1), respectively), but they display the same direction of motion for B_1 modes (i.e., vibration vectors of (0, 0, 1) and (0, 0, 1), respectively). On the basis of this rule, using the calculated vibrational patterns (Figure S3),

the Raman modes have been identified, as shown in Figure S2c and d. Importantly, in the backscattering configuration, the B_1 and B_2 modes cannot be observed in the experimental Raman spectra. It is worth noting that there is a deviation for identifying the 133 cm^{-1}, 456 cm^{-1}, and 501 cm^{-1} between our results and the results of Ref 3[3]. According to the theoretical results of polarization Raman spectra, as shown in Figure S4 and Figure 2 of Main Text, the A_2 modes exhibit four-leaf shapes with the maxima at 45°, 135°, 215°, and 315° under parallel configuration, and with the maxima at 0°, 90°, 180°, and 270° under cross configuration. Whereas the A_1 modes show two-leaf or four-leaf, or circle shapes, which depend on the values of a/b under parallel configuration, but show four-leaf shapes with the maxima at 45°, 135°, 215°, and 315° under cross configuration. In our measured polarization Raman spectra, the polarizing fitting curves of Raman peaks at 133 cm^{-1}, 456 cm^{-1}, 501 cm^{-1} wavenumbers (two leaves under parallel configuration and four leaves with the maxima at 45°, 135°, 215°, and 315° under cross configuration as shown in Figure 2 of Main Text and Figure S7) are in agreement with the simulated results. Therefore, in our discussion, these three peaks were identified as A_1 modes.

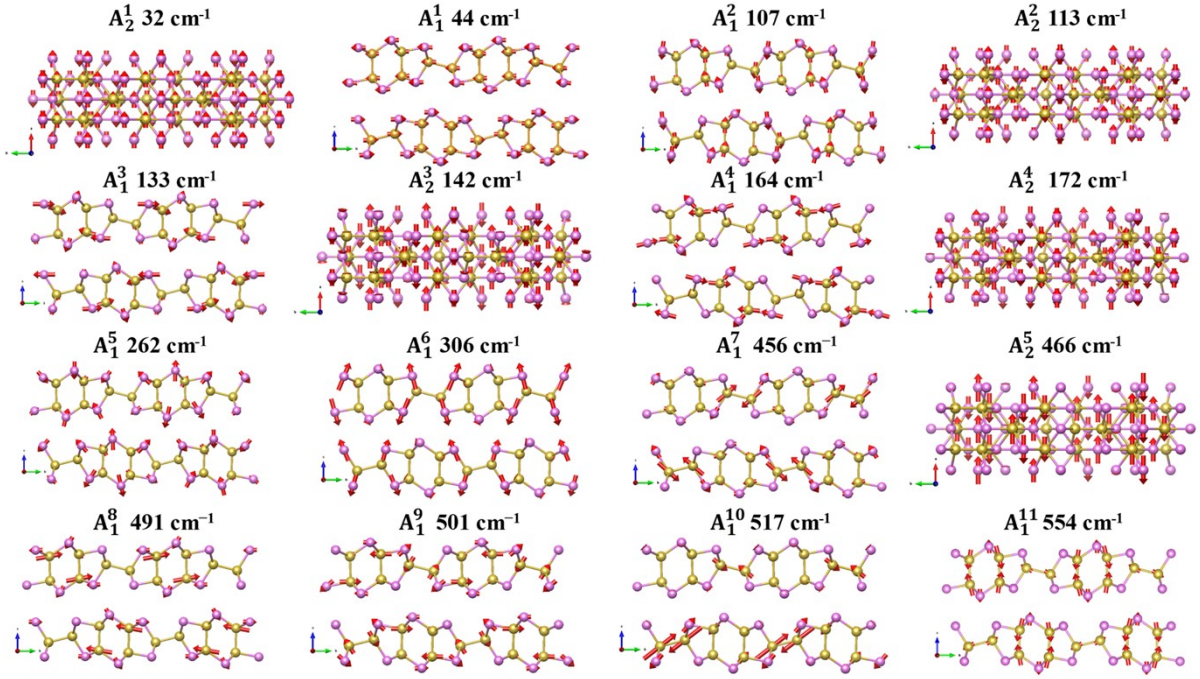

Figure S3. Calculated phonon vibration modes of bulk SiP. The red arrows represent the orientation of atomic vibration. The identified Raman modes and corresponding experimental

measured wavenumber are shown on the top of vibration patterns, and the crystal orientations are shown in the lower left corner. The A_1 and A_2 modes have the vibrational direction in the b-c plane and along a direction, respectively. The yellow and pink balls denote the Si and P atoms, respectively.

Figure S2b shows the measured Raman spectra of SiP flakes (on Si and SiO_2 substrates; red and pink lines, respectively) and Si wafer (black line). In the Raman spectrum of Si wafer, it shows a Raman peak at 521 cm^{-1}, which is in agreement with the previous results[7]. While the Raman spectrum of SiP flakes measured on the Si substrate shows a Raman peak near 520 cm^{-1} with a broad linewidth. To explore whether this peak is the multiple peaks, the Raman spectrum of SiP flakes were measured on SiO_2 substrate to avoid the Si Raman peaks of 521 cm^{-1} wavenumbers. As shown in Figure S2b, the Raman spectrum of SiP flakes measured on the SiO_2 substrate displays a Raman peak at 517 cm^{-1}, implying that the peak near 520 cm^{-1} mixes A_1^{10} and Si Raman modes for the Raman spectrum on Si substrate. Fitting with the Lorentz function, two Raman peaks located at 517 cm^{-1} (green stuffer region) and 521 cm^{-1} (blue stuffer region) wavenumbers in the Raman spectrum of SiP flakes on Si substrate, which is in accord with the Raman spectra of SiP flakes on SiO_2 substrate and Si wafer on the corresponding wavenumber. Hence, the Raman peak near 520 cm^{-1} is the hybridization peak of A_1^{10} and Si Raman modes of 521 cm^{-1}.

3. Polarization Raman spectra of SiP flakes

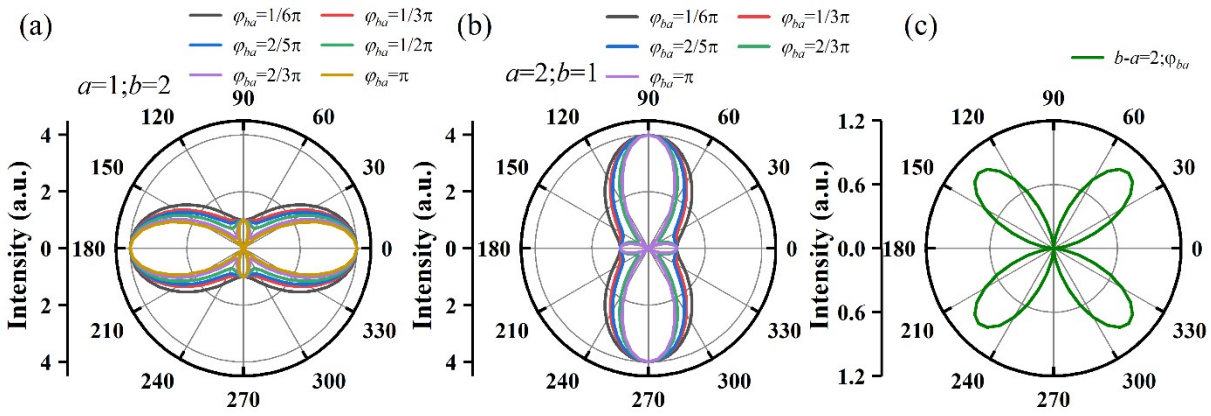

Figure S4. Simulated polarization-resolved Raman of A_1 modes. (a)-(b) The polarization

patterns with (a) $|b/a|$ >1 and (b) $|b/a|$ <1, as well as different φ_{ba} values under co-polarization configuration. The shape of simulated curves is the correlation to the values of b/a. (h) Polarization polar diagram with b-a = 2 and $\varphi_{ba} = 0$ under cross-polarization configuration.

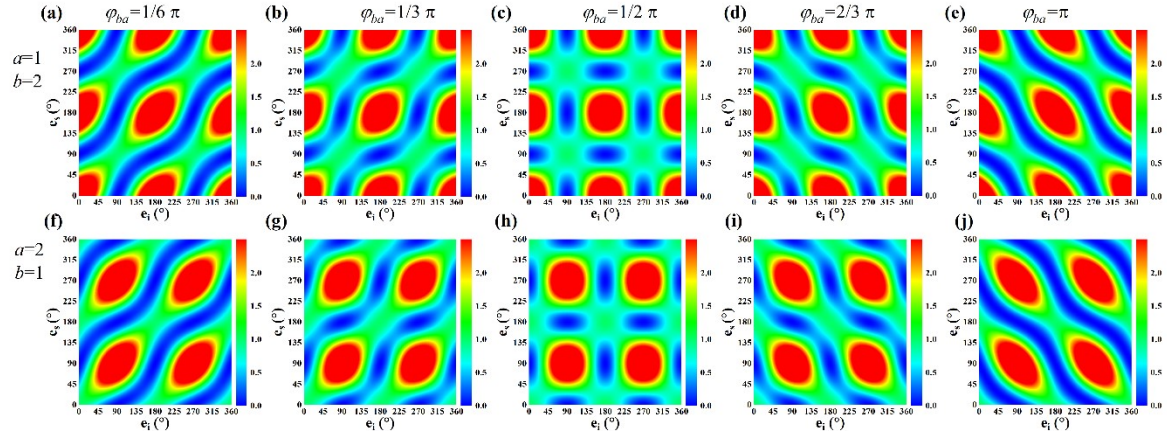

Figure S5. Simulated three-dimensional polarization Raman spectra for A_1 modes. (a)-(j) Angle-dependent polarization Raman spectra of A_1 modes for different values of a/b and φ_{ba}. $|b/a|$ >1 or $|b/a|$ <1 determines the island that locate at $\boldsymbol{e}_i/\boldsymbol{e}_s$=90°/90°, 90°/270°, 270°/90°, and 270°/270° or at $\boldsymbol{e}_i/\boldsymbol{e}_s$=0°/0°, 0°/180°, 180°/0°, and 180°/180°, while the shapes are variation with changing φ_{ba}.

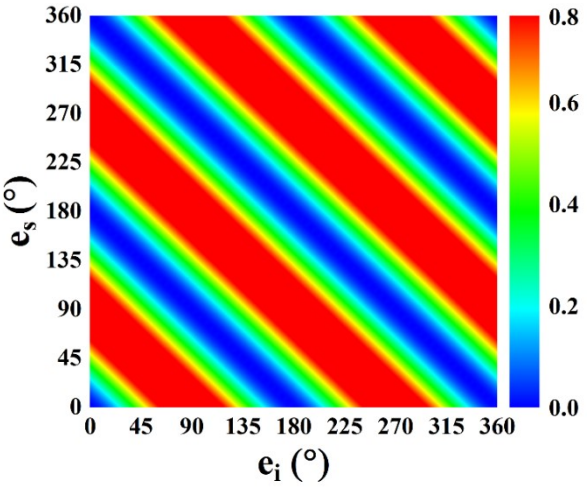

Figure S6. Simulated polarization Raman spectrum of A_2 modes for d=1 or d=-1. The simulated polarization spectrum of A_2 modes shows the four-line shapes with the orientation of [90° 90°] and [270° 270°] for any real number of d except for 0.

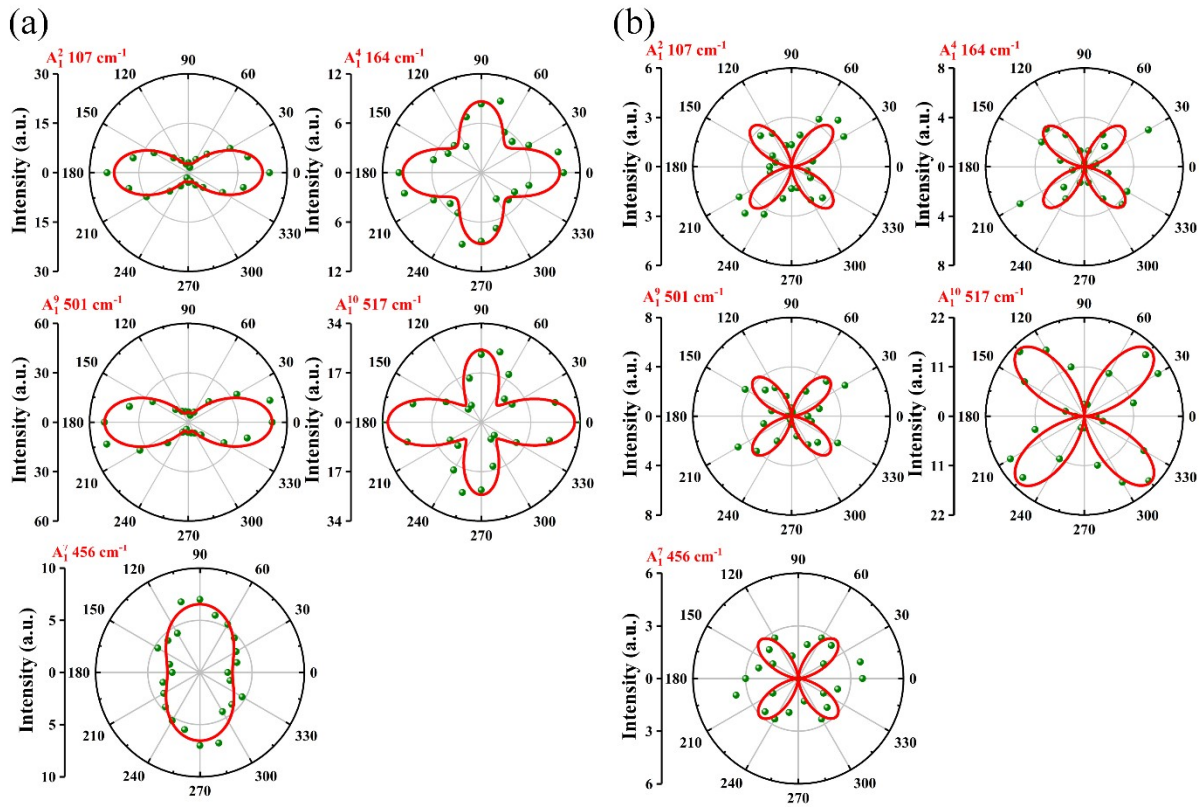

Figure S7. Experimental Raman polarizing feature of SiP flakes. Raman intensity as a function of polarization angle under (a) parallel and (b) cross polarization configuration for A_1^2, A_1^4, A_1^7 A_1^9 and A_1^{10} modes. The Raman intensity (green spheres) was extracted from the experimental Raman spectra and were fitted by eq. (5)-(8) of main text. Under parallel configuration, the Raman polarization spectra exhibit different shapes that depend on the values of $|\frac{b}{a}|$. Whereas only four-leaf shapes are observed, and the shapes are independent on the values of *a* and *b* under cross-polarization.

The Raman polarization patterns depend on the Raman tensor and the polarizing angle. Using the eq. (5)-(8) of Main Text, the polarization Raman spectra can be calculated. Figure S4 shows the simulated polarizing Raman spectra of A_1 modes with different values of *b/a* under co- and cross-polarization configuration. For A_1 modes of bulk SiP, under parallel polarization configuration, the fitting curves of Raman intensity are related to the *b/a* values. When $|b/a| > 1$ ($|b/a| < 1$), the curve exhibits a shape with the maximum at 0° and 180° (90° and 270°). With different φ_{ba} values, the secondary maximum show different shapes. As increase the phase

φ_{ba} from 0 to π, the secondary maximum gradually emerge and become narrow at $\varphi_{ba} = \pi$. Under cross-polarization configuration, the four-leaf shape is independent on the value of *a* and *b*. Regardless of the values of *b*-*a* (except for *b*-*a*=0), the polarization spectra show four-leaf shapes with the maximum at 45°, 135°, 215°, and 315° under cross configuration.

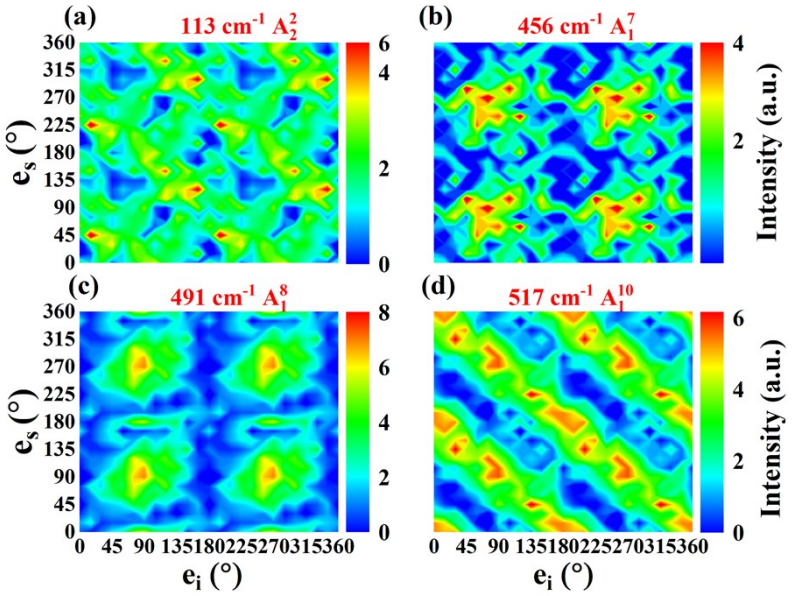

Figure S8. Experimental three-dimension polarizing Raman spectra of (a) A_2^2 (113 cm^{-1}), (b) A_1^7 (456 cm^{-1}), (c) A_1^8 (491 cm^{-1}), and (d) A_1^{10} (517 cm^{-1}). (a) and (d) show four lines along [180° 180°] and [360° 360°] direction, while (b) and (c) exhibit four islands located at $\boldsymbol{e}_i/\boldsymbol{e}_s$=90°/90°, 90°/270°, 270°/90°and 270°/270°, which is related to the values of *b*/*a*.

On the basis of the shapes of the curve, the $|\frac{b}{a}|$ value of A_1 modes can be quantitatively estimated. In our parallel-polarization Raman spectra (see Figure 2 of Main Text and Figure S7), A_1^1 (44 cm^{-1}), A_1^2 (107 cm^{-1}), A_1^3 (133 cm^{-1}), A_1^4 (164 cm^{-1}), A_1^5 (262 cm^{-1}), A_1^6 (306 cm^{-1}), A_1^9 (501 cm^{-1}), A_1^{10} (517 cm^{-1}), and A_1^{11} (554 cm^{-1}) exhibit two leaves with maxima at 0° and 180°, indicating the value of $|\frac{b}{a}|$ >1. However, A_1^7 (456 cm^{-1}) and A_1^8 (491 cm^{-1}) have the maxima at 90° and 270°, meaning the value of $|\frac{b}{a}|$ <1.

4. Sample-angle-dependent polarization Raman spectra of SiP flakes

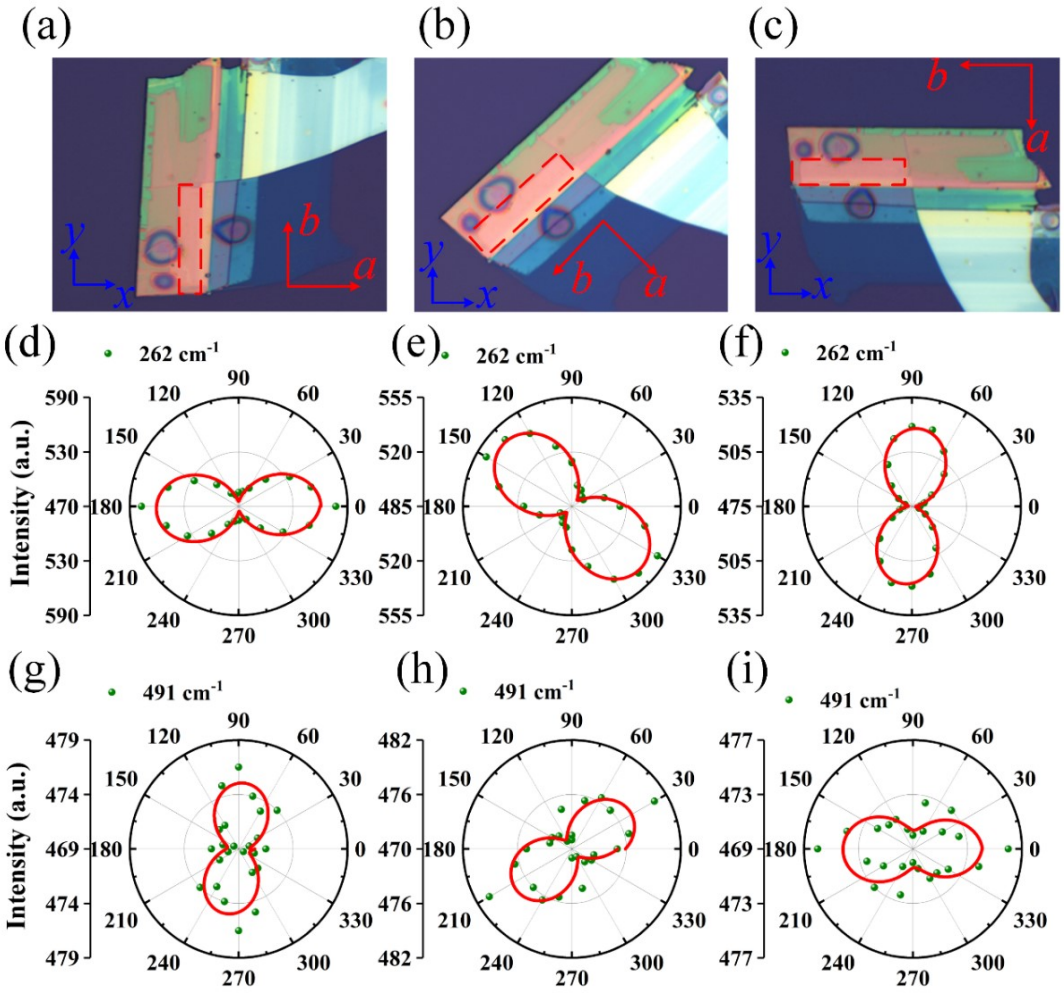

Figure S9. Angle-resolution Raman spectra of SiP flakes. (a)-(c) Optical image of SiP flakes with different sample positions. The blue and red coordinates represent the space coordinates of polarization light and crystal orientation coordinates, respectively. The measured azimuth of SiP flakes is (a) parallel (*a* is parallel to *x*), (b) intersecting at a 45° (the anele between *a* and *x* is 45°), and (c) cross (*a* is vertical to *x*) to the space coordinates. The red dotted frames denote the measured regions. Polarization Raman spectra with different azimuth angle of SiP sample for (d)-(f) 262 cm^{-1} and (g)-(i) 491 cm^{-1}. The linear dichroic orientations are robust dependent on the azimuth angle of SiP sample.

To identify the crystal orientation of SiP flakes, we measured parallel-polarization Raman spectra with different azimuth angle of SiP sample, as shown in Figure S9. According to polarization selection rules, in back-scattering configuration the A_1 modes can be distinctly observed when the polarization direction of incident and scattered light both along x or y

direction. For the A_1 modes with $|\frac{b}{a}| > 1$ ($|\frac{b}{a}| < 1$), the crystal direction *a* (*b*) is determined by the maximum of polarization Raman spectra. When the crystal position coordinate is consistent with the space coordinate, the polarization Raman spectra of 262 cm^{-1} ($|\frac{b}{a}| > 1$) exhibits the linear dichroism with a maximum at 0° and 180°, implying that the crystal orientation *a* is along *x* direction. With rotating the sample from 0° to 45° and then to 90°, the maximum of polarization Raman spectra of 262 cm^{-1} is from at 0° and 180° to 135° and 315° and then to 90° and 270°, indicating that the crystal orientations are robust dependent on the linear dichroic directions of polarization Raman spectra of A_1 modes. Those cases of 491 cm^{-1} are contract to 262 cm^{-1} due to its $|\frac{b}{a}| < 1$, as shown in the Figure S9. Thus, using the polarization Raman spectra, the crystal orientations are directly identified.

5. AFM and thickness-dependent PL spectra of SiP flakes

To determine the thickness of the SiP sample, the atomic force microscope (AFM) was measured. The AFM image is shown in Figure S10 (b). By measuring the height along red and blue dotted lines in Figure S10(b), the thicknesses from top to bottom in (a) are 2.87, 5.09, 6.13, 44.09 nm, respectively. Meanwhile, their PL and Raman spectra were measured. As shown in Figure S10 (a) and (b), the PL peak energy decrease with increasing thickness of SiP samples, which is in accord with the previous experimental[3] and theatrical[8] results. To further study the PL features under the different thickness of SiP samples, we manufactured the sample of SiP with different thicknesses, as shown in Figure S11a. With the order of B1, B2, B3, B4, and B5 (white dotted frames), the thickness increase. It can be seen from Figure S11b that the energy of PL peaks reduced with increasing the thickness of SiP which is consistent with the previous works[3]. This is attributed to the decreased band gaps with thickness increase[8], as shown in the calculated band gaps (1L, 2L, 3L, 4L, and bulk; Figure S11d). Additionally, when the thickness of SiP flakes increases, these PL intensities become more robust due to the enhanced cross-sectional optical absorption or emission, in accord with the observed phenomenon by Zhao et al.[3]. This thickness-dependent PL peaks intensity relationship of SiP is opposite to that of WSe_2[9, 10] which show a decreased strength with the thickness of samples increased due to the

enhanced dielectric screening[11-13]. Furthermore, the thickness-dependent Raman spectra show that the Raman peaks of few-layer SiP is weaker than multilayer SiP (Figure S10 f).

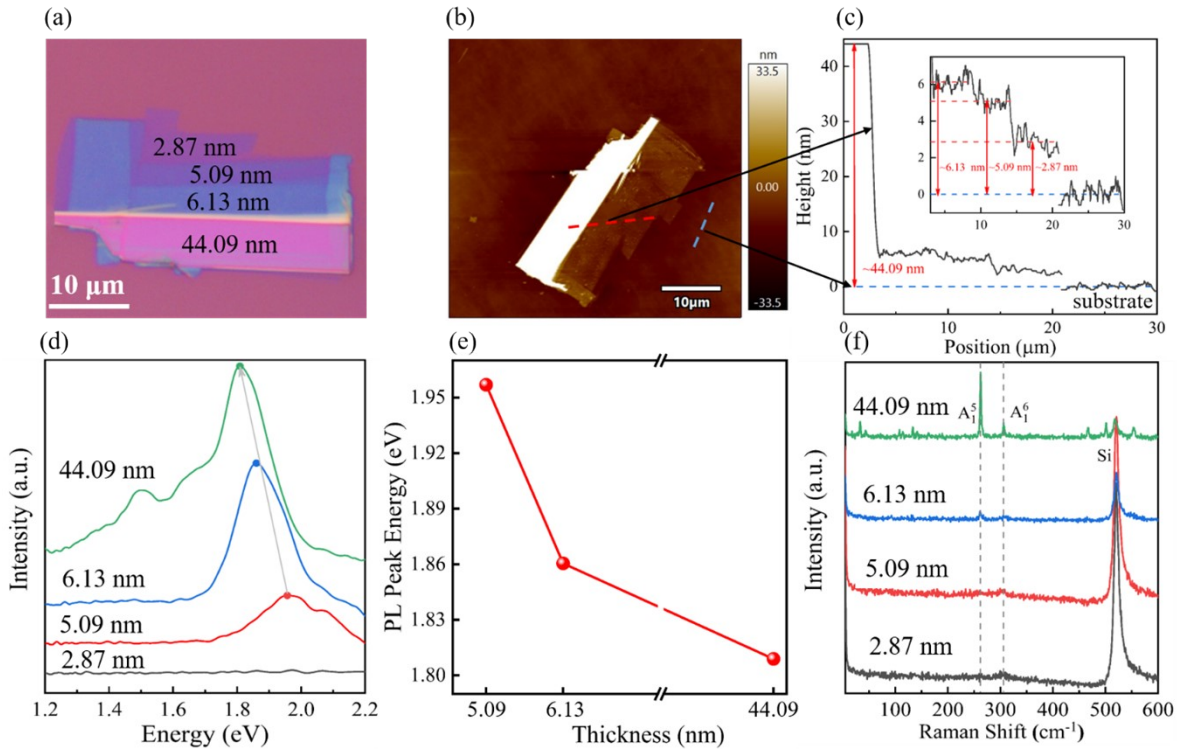

Figure S10. AFM of SiP flakes. (a) Optical image of SiP flakes with different thickness. The corresponding thickness estimated from (c) were marked. (b) AFM image of SiP flakes. (c) Sample heights along red and blue dotted lines in (b). The inset is sample heights of sample position from 3 μm to 30 μm. (d) Thickness-dependent PL spectra. The points are PL peak positions and the gray dotted line is used to guide the eyes. (e) PL peak energy as a function of thickness. (f) Thickness-dependent Raman spectra. The dotted lines represent A_1^5 and A_1^6 modes of SiP sample with thickness of 44.09 nm.

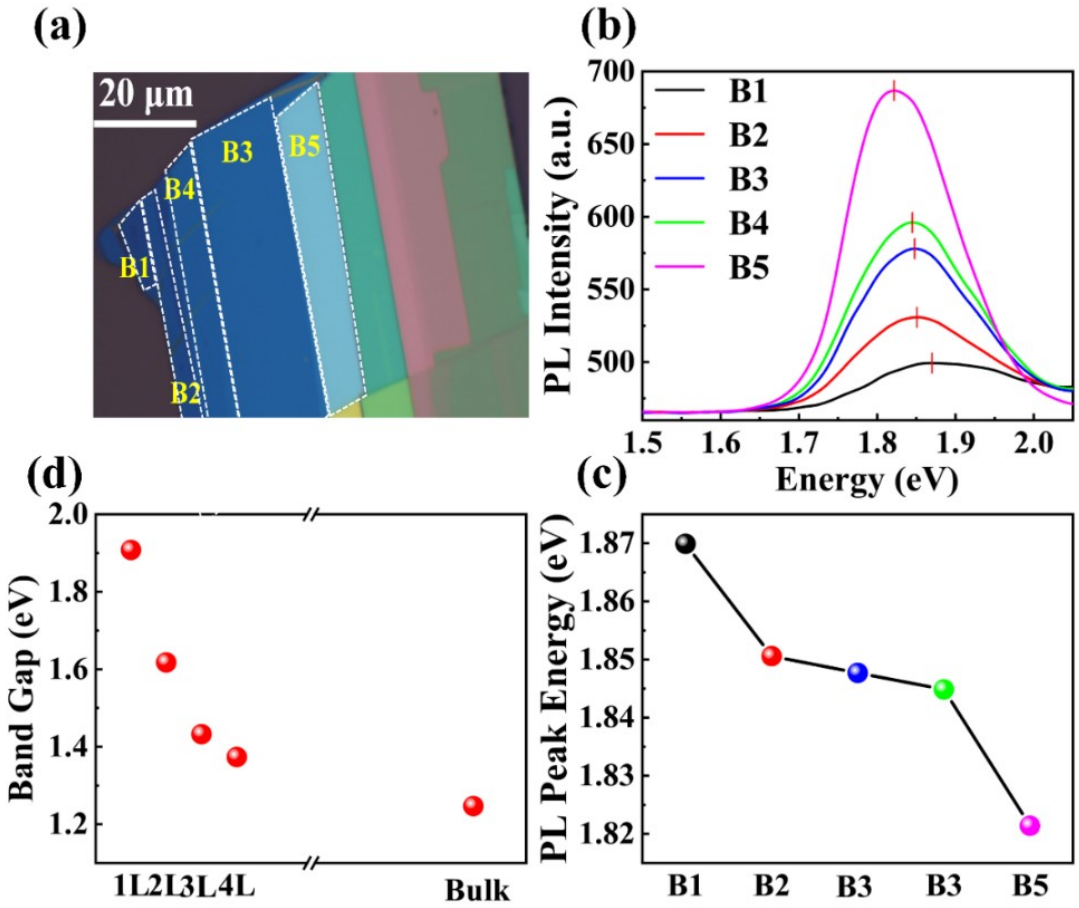

Figure S11. PL spectra of SiP flakes with thickness at room temperature. (a) Optical image of SiP flakes with different thicknesses. The white dotted frames represent the measured zones which are labeled as B1-B5. The thickness increase with the order of B1, B2, B3, B4, and B5. (b) PL spectra of B1-B5. The short red lines denote the PL peak position. (c) The energy of PL peak as a function of the measured area of B1-B5. The PL peaks show a redshift with the order of B1 to B5. (d) Calculated band gap of SiP as a function of the number of layers (1L, 2L, 3L, 4L, and bulk). The calculated band gaps are in agreement with the previous calculated results[8, 14, 15]. The band gaps decrease as increasing the number of layers.

6. Temperature-dependent PL spectra of SiP flakes

Figure S12a shows three measured zones encircled by the green, red, and blue dotted frames which were labeled as Z1, Z2, and Z3. For the Z3, at 15 K temperature, two indirect exciton (IX) and one neutral exciton (X_A) can be observed while the X_{B1} cannot be observed, which is different from the case on Z1 (Figure S14a) and Z2 (Main Text, Figure 4a). The lowest-energy

emission (X_p) was identified as the phonon sidebands similar to the case of layered SiP_2[16]. As increasing the temperature, the energy of IX_1, IX_2 X_p, and X_A shows redshift behaviors. At 77 K, the X_{B1} peak can be seen, with a trend of blueshift (Figure S12). For the Z1, the IX_2, X_p, X_A, and X_{B1} emissions show redshift behaviors, whereas the energy of IX_1 exhibits a redshift in the temperature range of 15-77 K and a blueshift in the 77-250 K temperature range, as shown in Figure S14c. In addition, the energy of X_{B2} emission (was observed beyond 150 K temperature) increases with the temperature increase, similar to that of Z2.

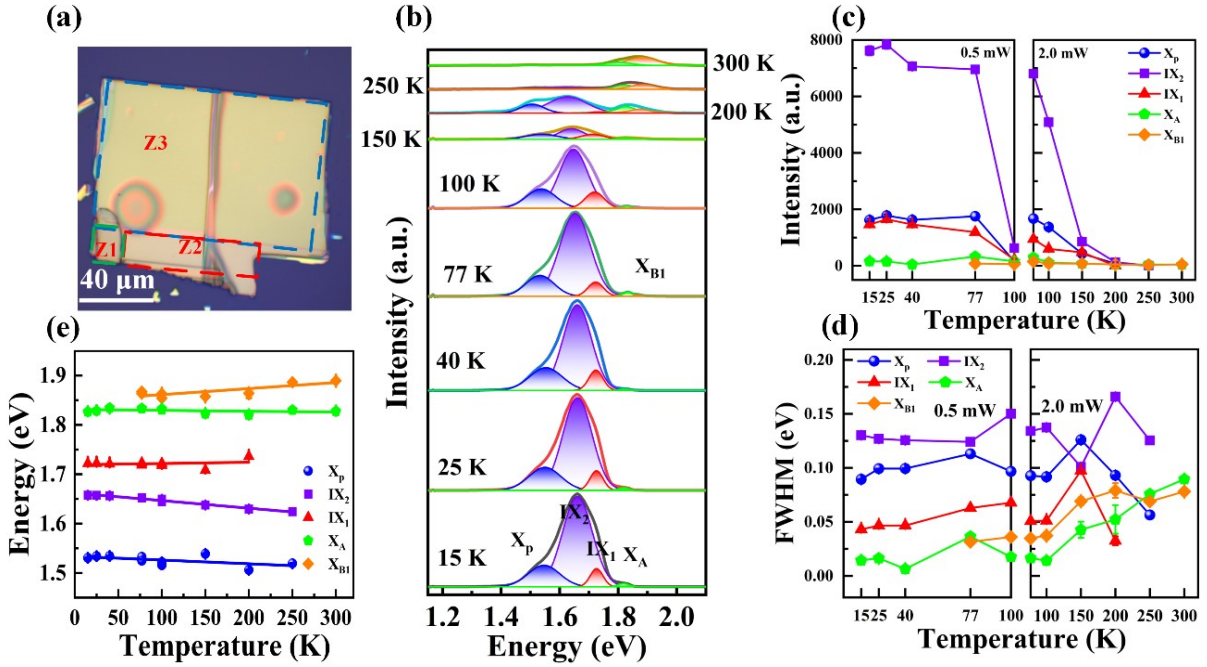

Figure S12. Temperature-dependent PL of SiP flakes. (a) Optical image of SiP flakes. The green (Z1), red (Z2), and blue (Z3) dotted frames represent three measured zones. (b) Temperature-dependent PL spectra of Z3. The solid lines and the filled regions denote the measured and fitting results, respectively. Four exciton emissions X_A, IX_1, IX_2, and Xp denote the neutral exciton, indirect exciton, indirect exciton, and phonon sideband, respectively. The high-energy emission emerging at 77 K is labelled as X_{B1}. Temperature-dependent (c) PL intensity and (d) full width at high maximum (FWHM) at laser power of 0.5 mW (left penal) and 2.0 mW (right penal). (e) Exciton emission energy as a function of the temperature. The energy of exciton peaks is extracted from the fitting results in (b).

We also studied the effect of pumping power on the exciton behaviour for Z1. As shown in

Figure S14d and S14e, the intensity of IX_2 and X_A increase with increasing the excitation power. Similar to the Z_2 (Main Text Figure 4), the IX_2 emission has a sublinear (α=0.36) relationship to laser power, indicating slower growth under higher excitation power. However, the intensity of X_A grows superlinearly (α=1.28), suggesting more exciton emission under high pumping power. Furthermore, the X_A exhibit linear dichroism with the maximum along 0° and 180° under parallel configuration and along 90° and 270° under cross configuration, behaving the same linear dichroism phenomenon as IX_2.

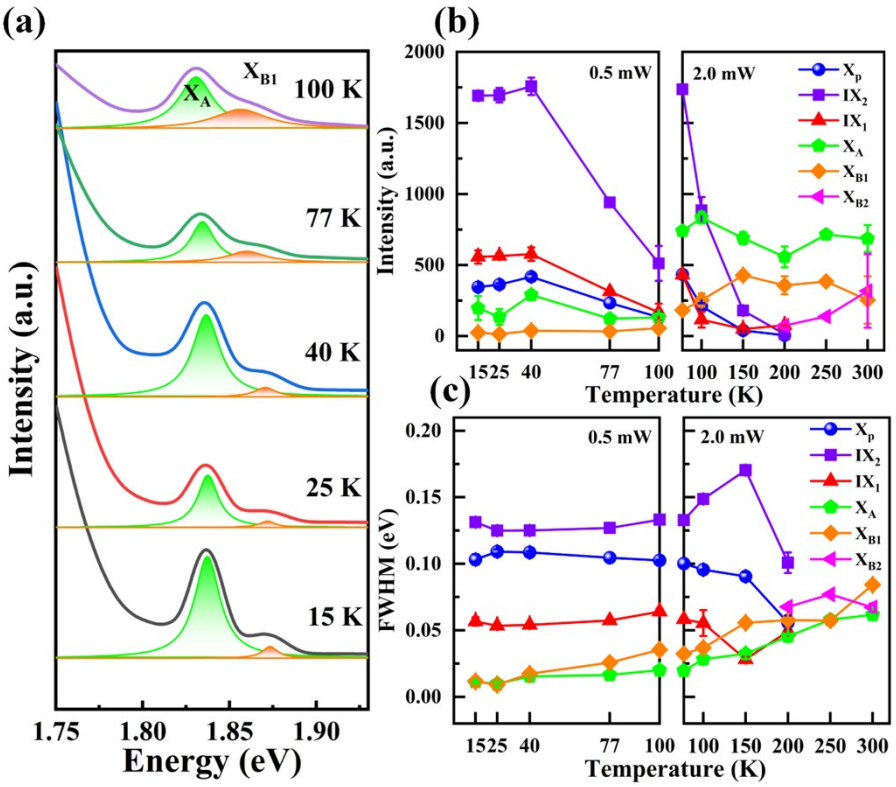

Figure S13. Temperature-dependent PL spectra of Z2. (a) PL spectra with X_A (green-filled regions) and X_{B1} (orange-filled regions) peaks in the temperature range of 15-100 K. The solid lines and the filled regions represent the measured and fitting results, respectively. (b) PL intensity and (c) full width at high maximum (FWHM) at laser power of 0.5 mW (left penal) and 2.0 mW (right penal) as a function of temperature.

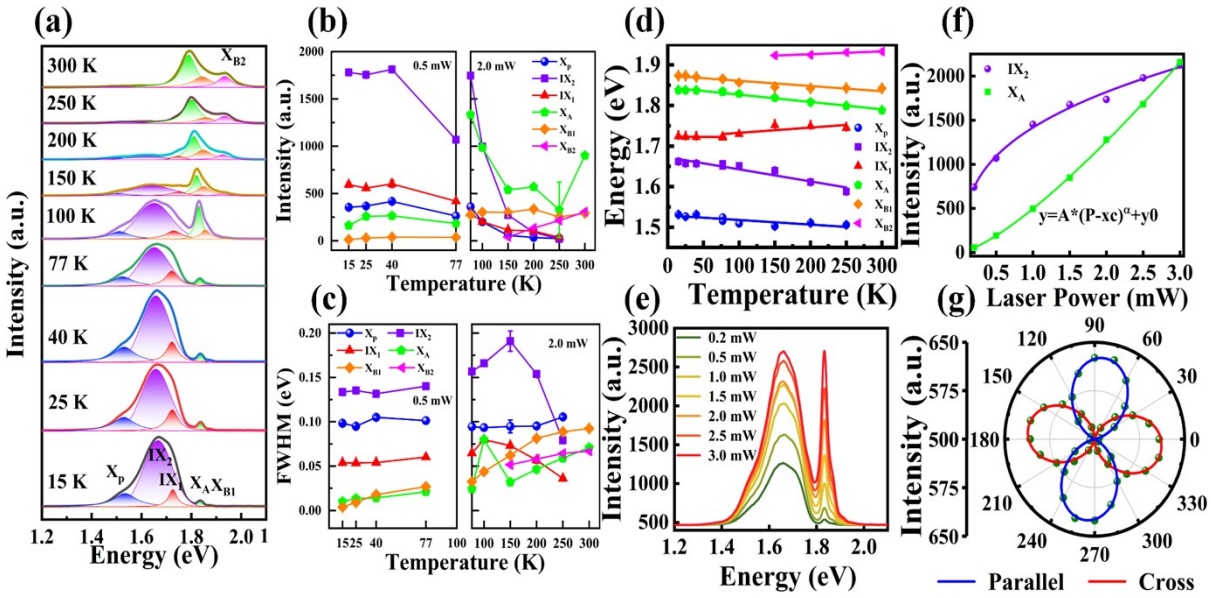

Figure S14. Temperature-dependent PL of SiP flakes. (a) PL spectra of Z1 as a function of the temperature from 15 K to 300 K. Temperature-dependent (b) PL intensity and (c) FWHM of SiP flakes at laser power of 0.5 mW (left penal) and 2.0 mW (right penal). (d) Energy of PL peaks extracted from the fitting results in (a) as a function of the temperature. (e) Power-dependent PL spectra were measured at 77 K in the laser power from 0.2 mW to 3.0 mW. (f) Power-dependent peak intensity of X_A and IX_2 extracted from (e). The purple and green splashes represent the experimental intensities of X_A and IX_2, respectively. The solid lines represent the fitting curves using the function of $y=A*(P-xc)^{\alpha}+y0$, where the P and α denote the laser power and index parameters, respectively. The power parameters α were 1.28 and 0.36 for X_A and IX_2, respectively. (g) Polar diagrams of polarization resolved X_A emission measured from Z3 under parallel (red line) and cross (blue line) configuration at 15 K. The green balls and the color lines (blue line under parallel configuration and red line under cross configuration) represent the experimental PL results and the fitting results using $\sin\theta$ function under polarization configuration, respectively.

7. Interplay-distance-dependent transition band gaps of bulk SiP

To investigate the effects of interplay coupling for the transition band gaps, we controlled the interplay distances (*d*, the distance between the nearest layer, see Figure S15a) of bulk SiP by changing the lattice constant *c*. Before calculating the interplay-distance-dependent band

structures, the lattice constants were fixed, and the atomic positions were relaxed. We enlarged the *c* by 1%, 3%, 5%, and 10%, and obtained the *d* with the corresponding change rate of 2.9 %, 9.1 %, 15.0 %, and 30.4 %. The corresponding *c* and *d* were listed in Table S2. As shown in Figure S15b, the transition band gaps of Λ-Ω, Γ-Ω, Γ-Γ, Z-Z, and X-X shift to blue, indicating that the weak interplay coupling increases the transition band gaps.

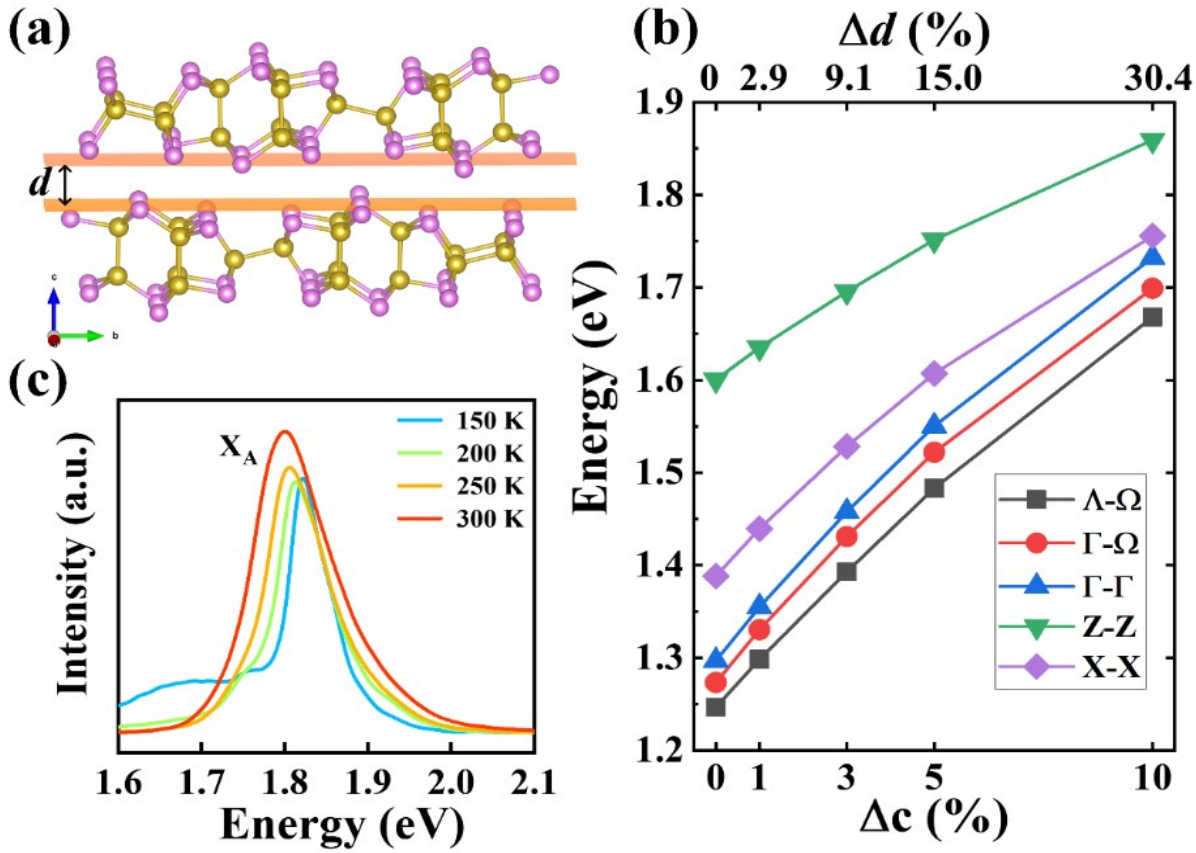

Figure S15. (a) Crystal structure of SiP. The *d* represents the nearest interplay distance, and the orange planes guide for the eye. The yellow and pink balls represent the Si and P atoms, respectively. (b) Optical transition bandgaps as a function of the Δc=(*c*-*c*0)/*c*0*100% (Δ*d*=(*d*-*d*0)/*d*0*100%), where *c* and *c*0 (*d* and *d*0) are the lattice constant (interplay distance) under strain and relaxation, respectively. The energy difference between the conduction band and valence band on the corresponding k-point shows increase trends. (c) The PL spectra of Z2 in the temperature range of 150-300 K. The X_A emission shows a high-energy asymmetry tail.

Table S2. Calculated out-of-plane lattice constant *c* and interplay distance *d* under strain. The $\Delta c=(c-c0)/c0*100\%$ and $\Delta d=(d-d0)/d0*100\%$ are the change ratio, where c / $c0$ and d / $d0$) are the lattice constant and interplay distance under strain/relaxation, respectively. The units of c and d are Å.

Δc	**0**	**1.0**	**3.0**	**5.0**	**10.0**
c	**13.781**	**13.919**	**14.195**	**14.470**	**15.160**
d	**2.175**	**2.239**	**2.372**	**2.502**	**2.836**
Δd	**0**	**2.9**	**9.1**	**15.0**	**30.4**

8. Absorbance anisotropic properties of SiP flakes

Table S3. Absorbance anisotropic ratio (Ani) of different in-plane anisotropic 2D materials. The Ani of black phosphorus (BP), ReS_2, and SnSe were estimated using the measured data of Yuan et al.[17], Liu et al.[18], and Yang et al.[19], respectively. The Ani in bracket represent the different measured data under 388 nm.

systems	BP[17]	ReS_2[18]	SnSe[19]	GeAs[20]	$PdSe_2$[6]	GeSe[21]	SiP (this work)
Ani	532 nm: **2.78**	514 nm: **1.34** 633 nm: **1.73** 785 nm: **3.02**	532 nm: 1.28 660 nm: **1.38**	520 nm: **1.14** 623 nm: **~1.00** 830 nm: **1.42**	364 nm: **1.11** 532 nm: **1.15** 633 nm: **1.19**	532 nm: **1.09** 638 nm: **1.26** 808 nm: **3.02**	388 nm: **1.16 (1.04)** 532 nm: **1.15** 733 nm: **1.19**

The absorbance anisotropic ratio (Ani) of SiP flakes and some typical 2D anisotropic materials are listed in Table S3. The Ani of SiP flakes is 1.16 at 388 nm, 1.15 at 532 nm, and 1.19 at 733 nm, exhibiting the anisotropy on absorbance. At 532 nm or near 532 nm wavelength (514 nm for ReS_2 and 520 nm for GeAs), SiP flakes has similar Ani relative to GeAs, $PdSe_2$ and GeSe, while has smaller Ani than BP, ReS_2, and SnSe. Additionally, in the Table S3, ReS_2 and GeSe have the highest Ani of 3.02 at 785 nm and 808 nm wavelength, respectively, showing

strong anisotropic absorbance property.

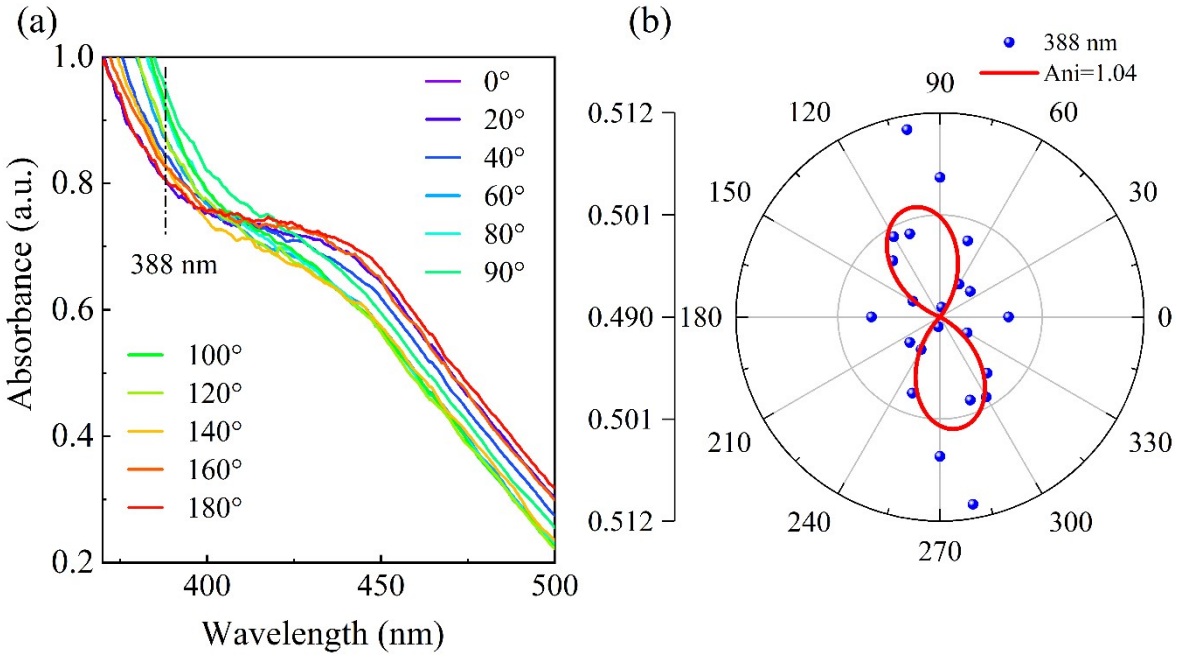

Figure S16. Absorption spectra of SiP flakes. (a) Polarization-dependent absorption spectrum of SiP flakes under parallel configuration. (b) Polar diagrams of absorbance at wavelengths of 388 nm. The Ani is 1.04.

9. Mechanical properties of bulk SiP

To export the mechanical properties of SiP materials, we calculated the elastic constants, elastic moduli, and Vickers hardness of bulk SiP. The elastic constants were calculated using strain-stress methods implemented in VASP, and the bulk modulus, shear modulus, and Young's modulus were obtained using Voigt-Reuss-Hill approximation[22-24]. To estimate the hardness of bulk SiP, the equation of Vickers hardness developed by Chen et al. [25] was adopted:

$$H_v = 2(\kappa^2 G)^{0.585} - 3 \quad (1)$$

Where the Pugh ratio κ=G/B. The theoretical results are listed in Table S3. It can be seen from Table S3 that the bulk SiP exhibits weak mechanical properties. Since the adjacent layers of layered SiP material are coupled by the van der Walls interaction along out-of-plane, its elastic constant of C_{33} (20.8 GPa) is much weaker than the C_{11} and C_{22}, implying the weaker resistant to normal strain along [001] direction relative to that along [100] and [010] direction. Moreover, the C_{66} is larger than C_{44} and C_{55}, which is attributed to the strong in-plane Si-P and Si-Si

covalent bonds. This indicates the stronger resistant to the shear strain along [110] direction compared to that along [101] and [011] directions. Whereas bulk SiP has low bulk, shear, and Young's moduli, suggesting weak performance against volume change, shear and tensile deformations. Unexpectedly, the bulk SiP show brittleness due to its κ=0.73>0.57.

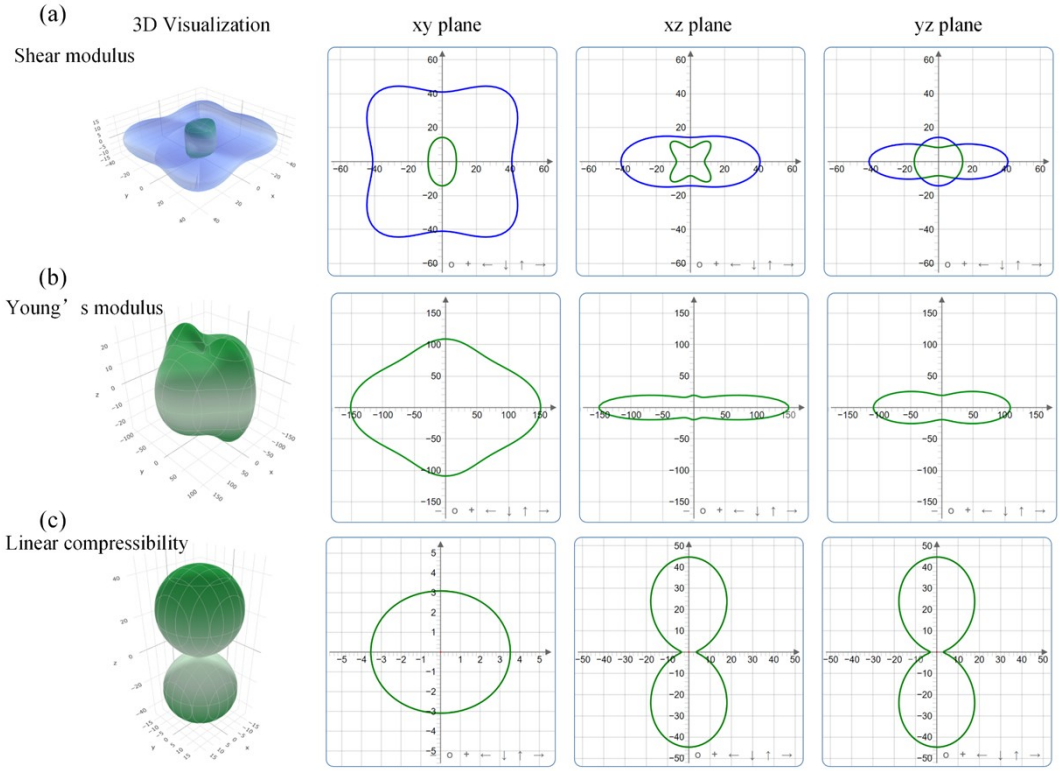

Figure S17. Anisotropic mechanical properties of bulk SiP. 3D visualization and its projections onto xy, xz, and yz planes for (a) shear modulus, (b) Young's modulus, and (c) linear compressibility. For the shear modulus, the blue and green surfaces (curves) represent the maximal and minimal isosurface. The anisotropic degree in xy plane (in-plane) is smaller than that in xz and yz plane for among shear modulus, Young's modulus, and linear compressibility.

Furthermore, we investigated the anisotropic mechanical properties of bulk SiP by the 3D shear modulus and Young's modulus. The 3D visualization of moduli and its projected curves onto the xy, xz, and yz planes plotted by the Elastic tensor analysis code[26, 27] are shown in Figure S17. For shear modulus, it shows a moderate cross shape with the maxima along [11] or [$\bar{1}$1] direction for G_{max} (blue curve; oval with the maximum along [01] direction for G_{min}, green curve), distinct two-leaf shape with maximum along [10] direction for G_{max} (blue curve; cross

shape with the maxima along [11] or [$\bar{1}$1] direction for G_{min}, green curve), and four-leaf shape with maximum along [10] direction and second extrema along [01] direction for G_{max} (blue curve; two-leaf shape with maximum along [10] direction, green curve) for xy, xz, and yz plane, respectively. While Young's modulus exhibits an almost ellipse curve with the extrema along [10] and [01] direction and linear-dichroic curves with the maximum along [10] direction for xy and xz (zy) plane, respectively. Moreover, the 3D linear compressibility shows two ellipsoids sticking together, and its projections onto the xy and xz (yz) planes have an almost sphere shape and dumbbell-like shape. These data indicate that bulk SiP shows strong anisotropic mechanical properties, and its anisotropic values of shear modulus, Young's modulus, and linear compressibility are 6.74, 7.95, and 14.48, as shown in Table S3.

Table S3. Calculated elastic constants, moduli (bulk modulus B, shear modulus G, and Young's modulus E), and Vickers hardness H_v (the unit is GPa). The unit of linear compressibility is TPa^{-1}. B_H, G_H, and E_H represent the estimated moduli using the Hill method. The anisotropic is obtained by the ratio of max to min values.

	C_{11}	C_{22}	C_{33}	C_{44}	C_{55}	C_{66}	G/B	v	H_v
Value	157.4	118.3	20.8	14.3	8.3	41.0	0.73	0.206	5.6
	B_H	Shear modulus			Young's modulus			Linear compressibility	
		G_H	G_{min}	G_{max}	E_H	E_{min}	E_{max}	β_{min}	β_{max}
Value	31.0	22.7	8.3	56.0	54.8	19.0	151.3	3.1	44.7
Anisotropic			6.74			7.95		14.48	

10. Samples of SiP flakes

To study the Raman, PL, and absorption spectra of SiP flakes, we fabricated four samples, as shown in Figure S18. The thickness of measured samples for temperature-dependent PL, absorption, and 3D polarization Raman spectra are bulk, few-layer, and multilayer, respectively. Whereas, for Raman polarization, the sample of multilayer thickness was measured, as shown in the pink region within yellow frame of Figure S18b. In addition, the thickness-dependent PL spectra were obtained by measuring the few-layer sample within red

frame and multilayer sample of shallow blue region within yellow frame of Figure S18b.

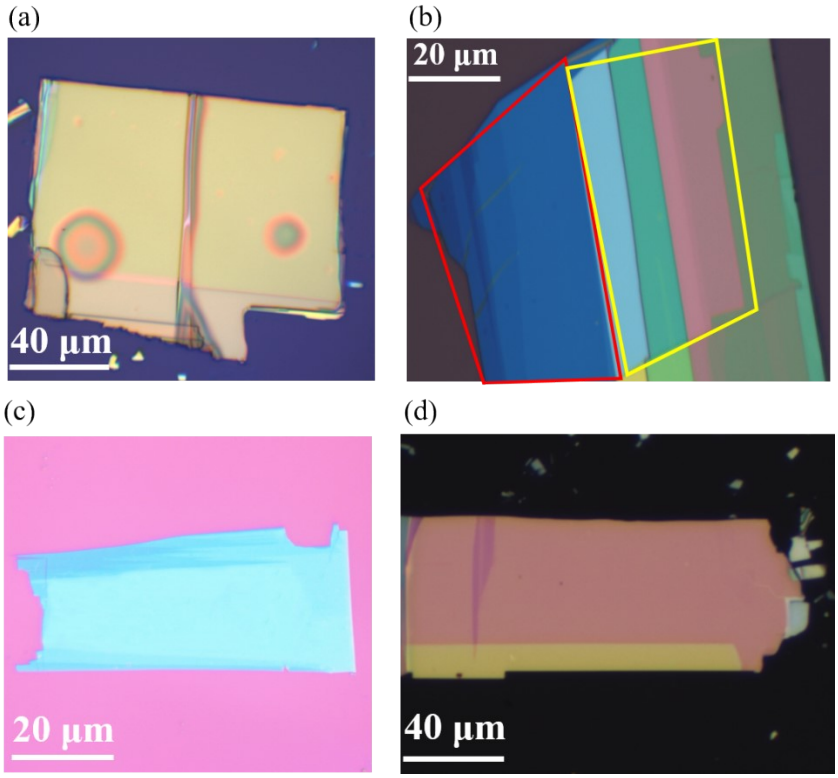

Figure S18. Samples of SiP flakes. Optical image of samples of SiP flakes for (a) temperature-dependent PL, (b) Raman polarization and thickness-dependent PL, (c) absorption, and (d) 3D Raman polarization spectra. The red and yellow solid frames in (b) represent the few-layer and multilayer thickness.

References

1. S. Grimme, S. Ehrlich, L. Goerigk, *J. Comput. Chem.*, 2011, **32**, 1456-1465.
2. S. Zhang, S. Guo, Y. Huang, Z. Zhu, B. Cai, M. Xie, W. Zhou, H. Zeng, *2D Mater.*, 2016, **4**, 015030.
3. S. Zhao, P. Luo, S. Yang, X. Zhou, Z. Wang, C. Li, S. Wang, T. Zhai, X. Tao, *Adv. Opt. Mater.*, 2021, **9**, 2100198.
4. S. Zhang, T. Yu, Y. Liu, M. Feng, X. Li, W. Sun, D. Wang, *Chem. Eng. J.*, 2022, **429**, 132248.
5. S. Geiskopf, A. Valdenaire, M. Stoffel, X. Devaux, E. André, C. Carteret, A. Bouché, M. Vergnat, H. Rinnert, *J. Phys. Chem. C*, 2021, **125**, 3235-3241.
6. J. Yu, X. Kuang, Y. Gao, Y. Wang, K. Chen, Z. Ding, J. Liu, C. Cong, J. He, Z. Liu, Y. Liu, *Nano Lett.*, 2020, **20**, 1172-1182.
7. J. H. Parker, D. W. Feldman, M. Ashkin, *Physical Review*, 1967, **155**, 712-714.
8. H. Shu, *Mater. Res. Express*, 2018, **6**, 026428.
9. D. Jeon, Y. Kang, T. Kim, *J. Phys. Chem. Lett.*, 2020, **11**, 6684-6690.
10. E. Easy, Y. Gao, Y. Wang, D. Yan, S. M. Goushehgir, E.-H. Yang, B. Xu, X. Zhang, *ACS Appl.*

Mater. Interfaces, 2021, **13**, 13063-13071.
11. G. Wang, A. Chernikov, M. M. Glazov, T. F. Heinz, X. Marie, T. Amand, B. Urbaszek, *Rev. Mod. Phys.*, 2018, **90**, 021001.
12. A. Chernikov, T. C. Berkelbach, H. M. Hill, A. Rigosi, Y. Li, B. Aslan, D. R. Reichman, M. S. Hybertsen, T. F. Heinz, *Phys. Rev. Lett.*, 2014, **113**.
13. X. Sun, Y. Zhu, H. Qin, B. Liu, Y. Tang, T. Lu, S. Rahman, T. Yildirim, Y. Lu, *Nature*, 2022, **610**, 478-484.
14. S. Kansara, P. D. Bhuyan, Y. Sonvane, S. K. Gupta, *J. Mater. Sci.*, 2019, **54**, 11878-11888.
15. Z. Guo, T. Wang, H. Liu, S. Qiu, X. Zhang, Y. Xu, S. J. Langford, C. Sun, *Nanoscale*, 2022, **14**, 5782-5793.
16. L. Zhou, J. Huang, L. Windgaetter, C. S. Ong, X. Zhao, C. Zhang, M. Tang, Z. Li, C. Qiu, S. Latini, Y. Lu, D. Wu, H. Gou, A. T. S. Wee, H. Hosono, S. G. Louie, P. Tang, A. Rubio, H. Yuan, *Nat. Mater.*, 2022, **21**, 773-778.
17. H. Yuan, X. Liu, F. Afshinmanesh, W. Li, G. Xu, J. Sun, B. Lian, A. G. Curto, G. Ye, Y. Hikita, Z. Shen, S. C. Zhang, X. Chen, M. Brongersma, H. Y. Hwang, Y. Cui, *Nat. Nanotechnol.*, 2015, **10**, 707-713.
18. F. Liu, S. Zheng, X. He, A. Chaturvedi, J. He, W. L. Chow, T. R. Mion, X. Wang, J. Zhou, Q. Fu, H. J. Fan, B. K. Tay, L. Song, R.-H. He, C. Kloc, P. M. Ajayan, Z. Liu, *Adv. Funct. Mater.*, 2016, **26**, 1169-1177.
19. S. Yang, Y. Liu, M. Wu, L.-D. Zhao, Z. Lin, H.-c. Cheng, Y. Wang, C. Jiang, S.-H. Wei, L. Huang, Y. Huang, X. Duan, *Nano Res.*, 2017, **11**, 554-564.
20. Z. Zhou, M. Long, L. Pan, X. Wang, M. Zhong, M. Blei, J. Wang, J. Fang, S. Tongay, W. Hu, J. Li, Z. Wei, *ACS Nano*, 2018, **12**, 12416-12423.
21. X. Wang, Y. Li, L. Huang, X. W. Jiang, L. Jiang, H. Dong, Z. Wei, J. Li, W. Hu, *J. Am. Chem. Soc.*, 2017, **139**, 14976-14982.
22. R. Hill, *Proc. Phys. Soc. London, Sect. A*, 1952, **65**, 349-354.
23. A. Reuss, *Zamm-J. Appl. Math. Mech.*, 1929, **9**, 49-58.
24. W. Voight, *Teubner, Leipzig*, 1928.
25. X.-Q. Chen, H. Niu, D. Li, Y. Li, *Intermetallics*, 2011, **19**, 1275-1281.
26. R. Gaillac, P. Pullumbi, F. X. Coudert, *J. Phys. Condens. Matter.*, 2016, **28**, 275201.
27. https://progs.coudert.name/elate.